Fault-Tolerant Control of Common Electrical Faults and Sensor Faults in Sensorless PMSM Drives

Yun Zhang, *Student Member, IEEE*, Xueqing Wang, *Senior Member, IEEE*, Lei Kong, *Student Member, IEEE*, Linlin Lu, *Student Member, IEEE*, Zheng Wang, *Senior Member, IEEE*, and Yao Mao, *Senior Member, IEEE*

***Abstract*—Conventional sensorless control can hardly estimate the rotor position of faulty drives, which will cause the breakdown of the sensorless permanent-magnet synchronous motor (PMSM) drives in short time. In this article, a fault-tolerant (FT) control scheme is proposed for common electrical faults and sensor faults in the sensorless PMSM drive without using any auxiliary facilities. In the proposed FT control scheme, by simply updating the voltage inputs in the nonlinear flux observer, the rotor position is accurately estimated in open-phase fault (OPF) and open-switch fault (OSF). With the aid of the estimated rotor position, the current references are optimized by considering the tracking error and torque ripple for OSF and OPF. Besides, a Luenberger observer based on stator voltages model is established to estimate the faulty phase current in current sensor fault. The FT control for voltage sensor fault is realized by compensating the measured dc-link voltage. Experimental verification is conducted to prove the validity of the proposed FT control scheme.**

***Index Terms*—Electrical faults, fault-tolerant control, nonlinear flux observer (NFO), sensor faults, sensorless permanent-magnet synchronous motor (PMSM) drive.**

I. Introduction

PERMANENT-MAGNET synchronous motor (PMSM) has been widely used in many applications, including industrial drives, home appliances, and electric vehicles, owing to its high power density, simple structure, and high efficiency [1], [3], [3], [4]. Due to the limited cost and space in some electrical applications, the sensorless control technology has become a hot research topic [5], [6]. On the other hand, the PMSM drives may suffer from various faults due to extreme operations and aging, which will cause safety problems and uncontrollable operations. The sensorless PMSM drives are more vulnerable to the faults since the sensorless control fails to estimate the rotor position in fault operations [7]. Therefore, it is necessary to investigate the fault-tolerant (FT) control of the sensorless PMSM drives.

Open-phase fault (OPF) and open-switch fault (OSF) are two common electrical faults, which will cause the breakdown of the sensorless PMSM drives. Many FT control schemes have been studied for OPF and OSF in motor drives [8], [9], [10], [11], [12], [13], [14], [15], [16], [17], [18], [19], [20], [21], [22]. For OPF, the FT control schemes can be fulfilled by adding auxiliary circuits [8], [9], [10], using open-winding configuration [11], [12], [13], and increasing phase number [14], [15]. In these FT control schemes, excellent FT performance can be obtained by establishing a new current path in OPF operations. In the aspect of OSF, OSF can be tolerated by adding the auxiliary circuits [16] and using the modified topologies with redundant switching states [17], [18]. In this way, the lost current path caused by the faulty switch can be reconstructed to improve the FT performance. Moreover, OSF can also be tolerated as OPF. Although the FT performance in motor drive can be improved by using the above mentioned FT control schemes under OPF and OSF, extra auxiliary circuits or complex topologies are required. It will introduce extra weight, volume, cost, and failure risk. To overcome these shortcomings, a few FT control schemes have been conducted to tolerate the OPF and OSF in the PMSM drive without using any redundant configurations [19], [20], [21], [22], [23]. It should be noted that the torque ripple is inevitable in OPF and OSF FT operations due to the loss of the faulty part. Nevertheless, the FT control of the sensorless PMSM drive is important for some high-reliability applications, such as electric vehicles, elevators, and aircraft. In these applications, continuous FT operation is required to move the system to safe zone. In [19], the FT control for OPF is realized by introducing a prefire angle during the current commutation in the PMSM drive. In this case, enough current commutation angle is guaranteed, which can eliminate the negative torque and reduce the current tracking error in OPF operation. In [20], an FT control of OSF is proposed based on the current prediction model in the PMSM drive. By using the current prediction model in OSF, the healthy voltage vector can be utilized maximumly, which can improve the sustainability of the torque output. In [21], both OPF and OSF are considered in the FT control of the PMSM drive. In the FT control, the second-order component is injected to replace the d-axis current reference after the phase currents reach their

Received 1 January 2025; revised 16 April 2025; accepted 22 May 2025. Date of publication 27 May 2025; date of current version 27 August 2025. This work was supported in part by the National Natural Science Foundation of China under Grant 62303333 and in part by Sichuan Science and Technology Program under Grant 2024JDRC0056. Recommended for publication by Associate Editor X. Li. *(Corresponding authors: Xueqing Wang; Yao Mao.)*

Yun Zhang, Lei Kong, Linlin Lu, and Yao Mao are with the National Key Laboratory of Optical Field Manipulation Science and Technology, Chinese Academy of Sciences, Chengdu 610209, China, also with the Key Laboratory of Optical Engineering, Chinese Academy of Sciences, Chengdu 610209, China, also with the Institute of Optics and Electronics, Chinese Academy of Sciences, Chengdu 610209, China, and also with the University of Chinese Academy of Sciences, Beijing 101408, China (e-mail: zhangyun21@mails.ucas.ac.cn; konglei@mails.ucas.ac.cn; lulinlin21@mails.ucas.ac.cn; maoyao@ioe.ac.cn).

Xueqing Wang is with the College of Electrical Engineering, Sichuan University, Chengdu 610065, China (e-mail: xwang@scu.edu.cn).

Zheng Wang is with the School of Electrical Engineering, Southeast University, Nanjing 210096, China (e-mail: zwang@eee.hku.hk).

Color versions of one or more figures in this article are available at https://doi.org/10.1109/TPEL.2025.3574040.

Digital Object Identifier 10.1109/TPEL.2025.3574040

boundaries, which can improve the torque performance and reduce the current tracking error. In [22], the excessive copper loss in the PMSM drives is considered in the FT control of OPF and OSF. By analyzing the relationship between torque and copper loss, the torque ripple is reduced as much as possible with the acceptable copper loss by introducing the appropriate copper loss ratio. However, the acquisition of the appropriate copper loss ratio is ignored. In [23], an FT control of OPF and OSF based on online current optimization is proposed in the PMSM drive. The *d–q* axis current references are optimized online by obtaining the appropriate copper loss ratio based on the calculation of the copper loss, which can obtain good balance between the torque ripple and the copper loss. The above FT control schemes possess good FT performance for OPF and OSF. However, they only focus on the PMSM drives with position sensors and are invalid for sensorless PMSM drives. Therefore, the FT control scheme of three-phase sensorless PMSM drive remains to be studied in OPF and OSF.

On the other hand, the sensorless PMSM drives are also vulnerable to the voltage-sensor fault (VSF) and the current-sensor fault (CSF). The common FT control schemes for VSF and CSF are realized by using the estimated information to replace the measured information of the faulty sensors in the sensorless motor drives [24], [25], [26]. In [24], a single-phase-current sensor FT control scheme for CSF is proposed in the sensorless PMSM drive, where the faulty current information is estimated by establishing a sliding-mode observer (SMO) based on the current space vector error reconstruction. Meanwhile, the current space vector error is selected as the correction term to improve the current estimation performance. In [25], the FT control scheme for CSF is realized by estimating the faulty current information based on the full-order SMO in the sensorless PMSM drive. In this scheme, the full-order SMO is established according to the full-order equations of PMSM. In [26], the FT control schemes of CSF and VSF are considered simultaneously in the sensorless PMSM drive, where the faulty current information and voltage information are estimated by using a high-order sliding mode observer and Luenberger observer, respectively. The CSF and VSF can be tolerated by using the estimated information to replace the faulty information in the sensorless PMSM drive. Although the above FT control schemes can fulfill excellent FT performance for CSF and VSF in the sensorless PMSM drives, only sensor faults are considered in these schemes. To improve the FT performance of the sensorless PMSM drive, the FT control schemes should consider as many faults as possible.

This article proposes an FT control scheme for OPF, OSF, CSF, and VSF in the sensorless three-phase PMSM drive without using any redundant configurations. After OPF and OSF, the α–β stator voltages of PMSM in faulty operations are calculated for the voltage inputs of the nonlinear flux observer (NFO) by establishing the relationship between the phase voltages and line voltages. In this way, the rotor position in OPF and OSF can be estimated. With the aid of the estimated rotor position, the *d–q* axis current references are optimized to reduce the current tracking error and torque ripple. For the CSF, the faulty-phase current is estimated by establishing the Luenberger observer based on the *d–q* stator voltages model. Besides, a voltage compensation based FT control is proposed for the VSF.

The rest of this article is organized as follows. Section II introduces the sensorless control of three-phase PMSM drive. The sensorless control of three-phase PMSM drive in fault operation is presented in Section III. In Section IV, the FT control scheme is proposed for OPF, OSF, CSF, and VSF. In Section V, the experimental results of the proposed FTC scheme are provided. Finally, Section VI concludes this article.

II. Sensorless Control of PMSM Based on the Nonlinear Flux Observer

A. PMSM Model

The electrical model of PMSM in synchronous reference frame can be expressed as

$$\begin{cases} u_d = R_s i_d + \frac{di_d}{dt} L_d - \omega_e L_q i_q \\ u_q = R_s i_q + \frac{di_q}{dt} L_q + \omega_e L_d i_d + \omega_e \psi_f \end{cases} \tag{1}$$

where L_d and L_q are the *dq*-axis inductances, i_d and i_q represent the *dq*-axis currents. R_s is the stator resistance. ψ_f is the PM flux linkage. ω_e denotes the electrical angular velocity.

The electromagnetic torque can be expressed as

$$T_e = \frac{3}{2} N_p (\psi_f i_q + (L_d - L_q) i_d i_q) \tag{2}$$

where N_p is the number of pole pairs.

B. Rotor Position and Speed Estimations Based on the NFO

In this article, the NFO is used to estimate the rotor position to realize the sensorless control in the PMSM drive, considering its advantages of high observing performance and simple implement [27]. The NFO for position estimation can be expressed as

$$\begin{cases} \dot{\hat{\psi}}_{s\alpha} = u_\alpha - R_s i_\alpha + \frac{\lambda}{2} \hat{\psi}_{r\alpha} \left[\psi_f^2 - \left| \hat{\psi}_r \right|^2 \right] \\ \dot{\hat{\psi}}_{s\beta} = u_\beta - R_s i_\beta + \frac{\lambda}{2} \hat{\psi}_{r\beta} \left[\psi_f^2 - \left| \hat{\psi}_r \right|^2 \right] \end{cases} \tag{3}$$

where i_α and i_β is the α–β stator currents, and L_s is the inductance. $\hat{\psi}_{s\alpha}$, $\hat{\psi}_{s\beta}$ and $\hat{\psi}_r$represent the estimated stator fluxes in α–β frame and the estimated rotor flux, respectively.

Meanwhile, the relationship between the estimated stator fluxs in α–β frame and the estimated rotor position can be expressed as

$$\begin{cases} \hat{\psi}_{s\alpha} = L_s i_\alpha + \psi_f \cos \hat{\theta}_e \\ \hat{\psi}_{s\beta} = L_s i_\beta + \psi_f \sin \hat{\theta}_e \end{cases} \tag{4}$$

where $\hat{\theta}_e$ is the estimated rotor position.

Then, the estimated rotor position can be solved as

$$\hat{\theta}_e = \tan^{-1} \left(\frac{\hat{\psi}_{s\beta} - L_s i_\beta}{\hat{\psi}_{s\alpha} - L_s i_\alpha} \right). \tag{5}$$

Based on the estimated rotor position, the rotor speed can be simply estimated by utilizing a typical tracking-controller-type speed estimator.

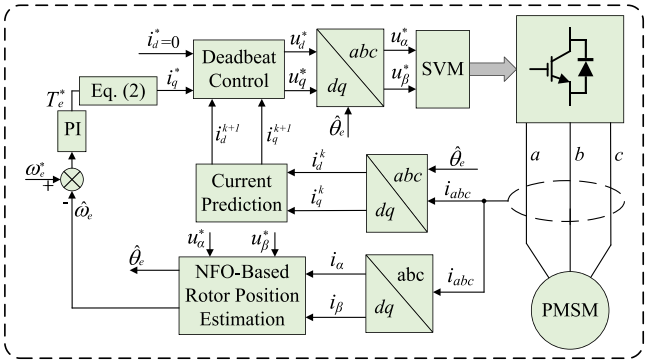

Fig. 1. Control diagram of the sensorless PMSM drive.

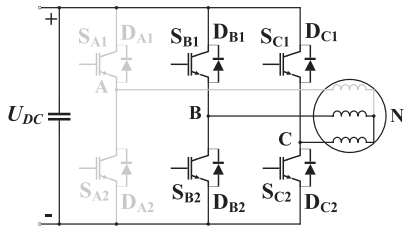

Fig. 2. PMSM drive with phase-A OPF.

C. Control Framework

Fig. 1 presents the established control diagram of the sensorless PMSM drive. In Fig. 1, the rotor position and speed of PMSM are estimated by using NFO. Based on the current prediction model and the deadbeat predictive current control, the *d*–*q* axis prediction currents are obtained to calculate the prediction voltage vector reference. In this way, arbitrary current reference patterns in the proposed FT control can be tracked quickly and precisely. Then, the space vector modulation is adopted to generate the switching state of the two-level voltage source inverter (VSI). In this article, the proposed FT control for OPF and OSF is realized by simply updating the voltage inputs of the NFO and *d*–*q* axis current references. For CSF, the faulty current information is replaced by using the estimated current to complete the FT control. The FT control of VSF is realized by compensating the measured dc-link voltage. In the proposed FT control scheme, the basic control framework will not be changed. Therefore, the control diagram in Fig. 1 also applies to the FT control of sensorless PMSM drive.

III. Sensorless Control of Faulty PMSM Drive

After a fault occurs, the operation conditions of the sensorless PMSM drive will be changed. As a result, the conventional sensorless control fails to estimate the rotor position in the faulty operations. However, the accurate rotor position is the foundation of FT control. Therefore, the effective sensorless control of the PMSM drive should be guaranteed in the faulty operations. In this article, the effective sensorless control of the PMSM drive is realized by simply updating the voltage inputs of the NFO in OPF and OSF operations. In this case, the accurate rotor position can be estimated in OPF and OSF operations. In CSF and VSF operations, the accurate rotor position can be estimated after introducing the FT control of CSF and VSF without changing the original sensorless control. Therefore, in this section, only the sensorless control for OPF and OSF in the PMSM drive will be considered.

In this article, the sensorless control can be divided into three conditions: healthy condition, faulty condition, FT condition. In healthy condition, the rotor position is estimated by using the NFO. In faulty condition, the OPF, OSF, CSF, and VSF are considered as the nonfatal faults and the PMSM drive will not breakdown immediately after these faults occur. Therefore, in faulty condition, the sensorless control can remain stable in a short period of time, and the estimated rotor position error is acceptable for the sensorless PMSM drive during the time. After these faults are diagnosed in short time, the sensorless PMSM drive enters the FT condition by introducing the proposed FT scheme. Generally, the OPF, OSF, CSF, and VSF can be diagnosed within a fundamental period [28], [29], [30]. Considering the short diagnosis time, the estimated rotor position error in the faulty condition is relatively small and acceptable for the sensorless PMSM drive before introducing the proposed FT scheme. Thus, the estimated rotor position in faulty condition can be used to calculate the desirable information of the proposed FT scheme before introducing the proposed FT scheme. After introducing the proposed FT scheme, the rotor position can be estimated accurately by updating the faulty model for NFO.

A. Sensorless Control in OPF Operation

In normal operation, the α–β stator voltage references and the α–β stator currents are selected as the inputs of the NFO to estimate the rotor position and speed, as shown in Fig. 1. In OPF operation, the current path of faulty phase will be blocked. Therefore, the actual α–β stator voltages will deviate from the α–β stator voltage references, which leads to the incorrect estimation of rotor position and speed. It can be seen from Fig. 1 that the α–β stator currents are obtained by measuring the three-phase currents, which can still be used to estimate the rotor position and speed in OPF operation. In summary, the actual α–β stator voltages should be obtained to estimate the accurate rotor position and speed in OPF operation. In this article, the actual α–β stator voltages are calculated by establishing the relationship between the phase voltages and line voltages in OPF operation. By using the calculated α–β stator voltages to updating the voltage inputs of the NFO, the accurate rotor position and speed can be estimated in OPF operation.

Taking phase-A OPF as an example, the current path of the fault phase will be blocked after phase-A OPF, and the motor is supported by the remaining two phases, as shown in Fig. 2. Therefore, the phase-A current will be forced to zero, and the change of switching states in phase-A VSI leg is not any influence for the PMSM control in phase-A OPF operation.

In normal operation, the Phase-A voltage model of the PMSM drive can be expressed as

$$u_{AN} = R_s i_A + L_s \frac{di_A}{d_t} - \psi_f \sin \hat{\theta}_e \hat{\omega}_e \tag{6}$$

where i_A is phase-A current. U_{AN} is phase-A voltage of the PMSM.

In phase-A OPF operation, the Phase-A current will be forced to zero. Therefore, (6) can be rewritten as

$$u_{AN} = -\psi_f \sin\hat{\theta}_e \hat{\omega}_e. \tag{7}$$

In Fig. 2, the phase-B and phase-C of the PMSM can be controlled normally in phase-A OPF. According to the relationship between the line voltage and the α–β stator voltage references, the line voltage between phase-B and phase-C can be obtained as

$$u_{BC} \approx \sqrt{3} u_\beta^*. \tag{8}$$

The line voltage between phase-B and phase-C can also be expressed as

$$u_{BC} = u_{BN} - u_{CN} \tag{9}$$

where u_{BN} and u_{CN} are the phase-B and phase-C voltages, respectively.

According to the Kirchhoff's voltage law, the three-phase voltages have the following relationships:

$$u_{CN} = -u_{AN} - u_{BN}. \tag{10}$$

By substituting (10) into (9), the line voltage between phase-B and phase-C can be rewritten as

$$u_{BC} = 2u_{BN} + u_{AN}. \tag{11}$$

By substituting (7) and (8) into (11), phase-B voltage can be solved as

$$u_{BN} \approx \frac{1}{2}(\psi_f \sin\hat{\theta}_e \hat{\omega}_e + \sqrt{3} u_\beta^*). \tag{12}$$

Then, by substituting (7) and (12) into (10), phase-C voltage can be calculated as

$$u_{CN} \approx \frac{1}{2}(\psi_f \sin\hat{\theta}_e \hat{\omega}_e - \sqrt{3} u_\beta^*). \tag{13}$$

By combining Clark transformation, (7), (12), and (13), the actual α–β stator voltages in phase-A OPF operation can be obtained in (14) after ignoring the inverter nonlinearity

$$\begin{cases} u_\alpha = -\psi_f \sin\hat{\theta}_e \hat{\omega}_e \\ u_\beta \approx u_\beta^* \end{cases}. \tag{14}$$

By using the calculated α–β stator voltages in (14) to update the voltage inputs of the NFO, accurate rotor position and speed can be estimated in phase-A OPF operation.

B. Sensorless Control in OSF Operation

The OSF can be divided into two types, namely upper switch and lower switch faults. In order to illustrate the fault characteristics of OSF, lower switch fault in phase-A, namely S_{A2}-OSF, is taken as an example. After S_{A2}-OSF, the configuration of faulty PMSM drive is changed, as shown in Fig. 3. It can be seen from Fig. 3 that only the current path of the faulty power switch will be lost and other current paths remain normal.

To present the influence of the current path in S_{A2}-OSF operation more clearly, the current path of Phase-A VSI leg

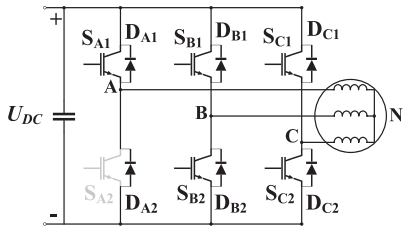

Fig. 3. PMSM drive with S_{A2}-OSF.

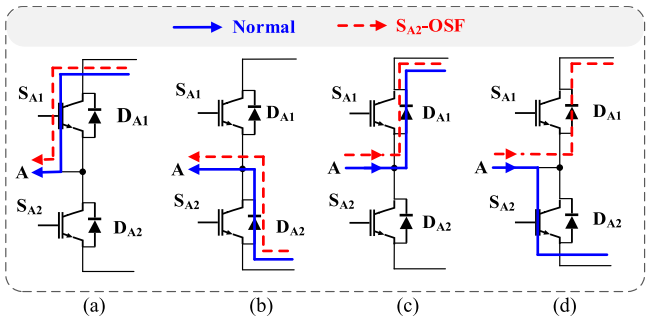

Fig. 4. Current paths under different switch states and current directions. (a) i_A>0; S_{A1} ON, S_{A2} OFF. (b) i_A>0; S_{A1} OFF, S_{A2} ON. (c) i_A<0; S_{A1} ON, S_{A2} OFF. (d) i_A<0; S_{A1} OFF; S_{A2} ON.

under the different current directions and switching states is presented in Fig. 4. In Fig. 4, the current path in normal operation is marked with the blue line. The red line represents the current path in S_{A2}-OSF operation. After S_{A2}-OSF, the current path of the lower switch S_{A2} is blocked. When the normal phase current flows through the diode and the upper switch S_{A1}, the operation state will not be influenced since the current of the faulty phase is not changed, as shown in Fig. 4(a), (b), and (c). When the normal phase current flows through the lower switch S_{A2}, the current has to flow to the diode D_{A2} to establish the new current path in the state of phase-A current inflow due to the loss of the current path in the lower switch S_{A2}, as shown in Fig. 4(d). As a result, after S_{A2}-OSF, phase-A current will be forced to zero in the negative half fundamental period, and the Phase-A current is normal in the positive half fundamental period. The same rule applies equally other OSFs.

In S_{A2}-OSF operation, the actual α–β stator voltages are still deviate from the α–β stator voltage references due to the loss of the current path in the lower switch S_{A2}, which will lead to estimation error of the rotor position in the NFO. Therefore, the acquisitions of the actual α–β stator voltages for the NFO in S_{A2}-OSF operation are also necessary to realize the effective senorless control in the PMSM drive. Based on the above analysis, the faulty phase current in S_{A2}-OSF operation can be considered as a combination of the normal phase current in healthy half fundamental period and zero current of phase-A OPF in faulty half fundamental period. As a result, the acquisitions of the actual α–β stator voltages can be divided into two modes. The first mode represents that the actual α–β stator voltages are equal to the α–β stator voltage references in the healthy half fundamental period. In the second mode, the

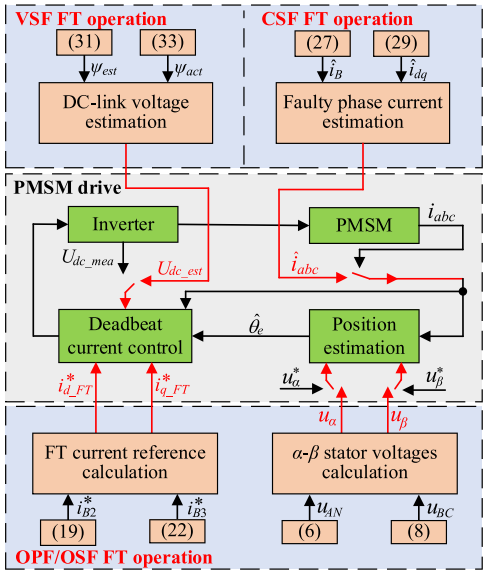

Fig. 5. Block diagram of the proposed FT control of sensorless PMSM drive.

actual α–β stator voltages can be calculated by using (14) in the faulty half fundamental period. Therefore, after ignoring the inverter nonlinearity, the actual α–β stator voltages in S_{A2}-OSF operation can be calculated as

$$\begin{cases} u_\alpha \approx \begin{cases} u^*_\alpha & (i_a > 0) \\ -\psi_f \sin\hat{\theta}_e \hat{\omega}_e & (i_a \le 0) \end{cases} . \\ u_\beta \approx u^*_\beta \end{cases} \tag{15}$$

By updating the voltage input of the NFO with (15), the effectiveness sensorless control of the PMSM drive can be ensured in S_{A2}-OSF operation.

IV. FT Control of Sensorless PMSM Drive

In this article, an FT control scheme is proposed for OPF, OSF, CSF, and VSF in the sensorless PMSM drive, as shown in Fig. 5. After OPF and OSF, the calculated α–β stator voltages are used to update the voltage input of the NFO, which can realize the effectiveness sensorless control. Then, the current commutation time is considered in the establishment of FT current reference to reduce the current tracking errors and torque ripple. For CSF, the faulty phase current is estimated by using the Luenberger observer to realize the FT control. By obtaining the estimated flux and actual flux, the dc-link voltage is estimated to tolerate the VSF.

A. FT Control for OPF

Based on the proposed sensorless control of faulty PMSM drive in Section III, the conventional FT control scheme for OPF can be used in sensorless PMSM drive. To obtain the theoretical minimum torque ripple in the phase-A OPF FT operation, the polarity of the phase-B FT current reference is changed immediately in [22], and the phase-B FT current reference can be denoted as

$$i^*_{B1} = \begin{cases} \frac{\sqrt{3}N_p\psi_f\cos\hat{\theta}_e + C_1}{N_p(L_d - L_q)} & (0 \le \hat{\theta}_e < \pi) \\ \frac{-\sqrt{3}N_p\psi_f\cos\hat{\theta}_e - C_1}{N_p(L_d - L_q)} & (\pi \le \hat{\theta}_e < 2\pi) \end{cases} \tag{16}$$

where

$$C_1 = \sqrt{3(N_p\psi_f\cos\hat{\theta}_e)^2 + 4N_p(L_d - L_q)\sin(2\hat{\theta}_e)T^*_e}. \tag{17}$$

For the surfaced-mounted PMSM ($L_d = L_q$), the Phase-B FT current reference can be simplified as

$$i^*_{B1} = \frac{T^*_e}{\sqrt{3}N_p\psi_f\cos\hat{\theta}_e}. \tag{18}$$

Moreover, the overcurrent endurance of the PMSM drive should also be considered in the phase-B FT current. Therefore, the new phase-B FT current reference can be expressed as

$$i^*_{B2} = \begin{cases} \min\{i^*_{B1}, I_{\max}\} & (i^*_{B1} > 0) \\ \max\{i^*_{B1}, -I_{\max}\} & (i^*_{B1} \le 0) \end{cases} \tag{19}$$

where $I_{\max}$ is the maximum amplitude of the phase current, and is set as 10A in this article.

According to (16) and (18), the current polarity should be changed immediately in the positions of $\pi/2$ and $3\pi/2$ to reach the theoretical minimization of torque ripple. However, the actual phase-B current cannot change abruptly due to the impact of motor inductance. As a result, the tracking error between the FT current reference and the actual current will be generated and the negative torque will be generated during current commutation. To eliminate the current tracking error, the desired current commutation time should be guaranteed during the current commutation. Smaller current commutation time will cause the current tracking errors and larger current commutation time will increase the torque ripple due to the decrease of the current contribution. Thus, the desirable current commutation time in this article is calculated according to (20) [19]

$$T_c \approx \frac{L_{bc} i_B}{U_{dc}} \tag{20}$$

where L_{bc} represents the inductance between the windings of phase-B and phase-C. i_B is the phase-B current.

According to the desirable current commutation time, after introducing a certain margin, the commutation starting angle and commutation stop angle near the position of $\pi/2$ and $3\pi/2$ can be calculated as

$$\begin{cases} \theta^-_{c1} = \frac{\pi}{2} - \hat{\omega}_e T_c, \theta^+_{c1} = \frac{\pi}{2} + \hat{\omega}_e T_c \\ \theta^-_{c2} = \frac{3\pi}{2} - \hat{\omega}_e T_c, \theta^+_{c2} = \frac{3\pi}{2} + \hat{\omega}_e T_c \end{cases} \tag{21}$$

where θ^-_{c1} and θ^-_{c2} are the commutation starting angle near the position of $\pi/2$ and $3\pi/2$, respectively. θ^+_{c1} and θ^+_{c2} are the commutation stop angle near the position of $\pi/2$ and $3\pi/2$, respectively.

In this article, the current pattern of a straight line with the fixed slope is introduced during the current commutation to realize the commutation starting angle and commutation stop angle in (21), and the phase-B FT current reference during the

current commutation is expressed as

$$i^*_{B3} = \begin{cases} \frac{I_{\max}}{2\hat{\omega}_e T_c}(\pi - 2\hat{\theta}_e) & \theta^+_{c1} \le \hat{\theta}_e \le \theta^-_{c1} \\ \frac{I_{\max}}{2\hat{\omega}_e T_c}(2\hat{\theta}_e - 3\pi) & \theta^-_{c2} \le \hat{\theta}_e \le \theta^+_{c2} \end{cases}. \tag{22}$$

Finally, the new phase-B FT current reference considering the current commutation is denoted as

$$i^*_{B4} = \begin{cases} \min\{i^*_{B2}, i^*_{B3}\} & (i^*_{B1} > 0) \\ \max\{i^*_{B2}, i^*_{B3}\} & (i^*_{B1} \le 0) \end{cases}. \tag{23}$$

Since the commutation starting angle and commutation stop angle are considered in the FT phase-B current $i*B4$, the desired current commutation angle can be can be guaranteed during the current commutation. In the positions of $\pi/2$ and $3\pi/2$ during the current commutation, both the FT phase-B current reference $i*B4$ and the FT torque reference $T*e\_FT$ will be zero. According to (23), Kirchhoff's law, and Park transformation, the FT d–q axis current references in phase-A FT OPF operation can be expressed as

$$\begin{cases} i^*_{d\_FT} = \frac{2\sqrt{3}}{3} i^*_{B4} \sin\hat{\theta}_e \\ i^*_{q\_FT} = \frac{2\sqrt{3}}{3} i^*_{B4} \cos\hat{\theta}_e \end{cases}. \tag{24}$$

By using the optimized d–q axis current references, the negative torque caused by the current commutation can be effectively eliminated compared to the conventional FT control and the torque ripple can be further reduced.

B. FT Control for OSF

As analyzed in Section III-B, the faulty phase current will be forced to zero under OPF. For OSF, the OSF can be divided into upper switch fault and lower switch fault. After the upper switch fault occurs, the current path of the upper switch is lost in the faulty phase. As a result, the positive current of the faulty phase can only flow through the freewheeling diode. Therefore, the positive current of the faulty phase will be forced to zero in the positive half fundamental period. The negative current of the faulty phase will not be influenced since it does not flow through the faulty switch. The same rules apply equally to the lower switch fault. Based on the above analysis, the current characteristics of OSF can be considered as a combination of half fundamental period in healthy state and half fundamental period in OPF state. As a result, OSF and OPF share similar fault characteristics in the faulty half fundamental period. Therefore, a two mode FTC is proposed for OSF. The FT Phase-B current in (23) applies equally to S_{A2}-OSF in the faulty half fundamental period. In the healthy half fundamental period, the healthy d–q axis current references are still used. Finally, the FT d–q axis current references in S_{A2}-OSF FT operation can be obtained as

$$\begin{cases} i^*_{d\_FT} = \begin{cases} i^*_d & (i_a > 0) \\ \frac{2\sqrt{3}}{3} i^*_{B4} \sin\hat{\theta}_e & (i_a \le 0) \end{cases} \\ i^*_{q\_FT} = \begin{cases} i^*_q & (i_a > 0) \\ \frac{2\sqrt{3}}{3} i^*_{B4} \cos\hat{\theta}_e & (i_a \le 0) \end{cases} \end{cases}. \tag{25}$$

C. FT Control for CSF

In this article, the current information of the faulty current sensor is estimated by establishing the Luenberger observer based on PMSM model in d–q coordinate system. Then, the current information from the faulty current sensor is replaced with the estimated current to tolerate the CSF. Typically, two current sensors are used in the PMSM drive. For better understanding, phase-A CSF is selected as an example to introduce the proposed FT control for the CSF. In phase-A CSF operation, the measured phase-B current is correct. By using the inverse Park transformation, the phase-B current can be denoted as

$$i_B = \cos\left(\hat{\theta}_e - \frac{2\pi}{3}\right) i_d - \sin\left(\hat{\theta}_e - \frac{2\pi}{3}\right) i_q. \tag{26}$$

By combining (1), (26), and the conventional Luenberger observer in [26], the Luenberger observer based on PMSM model in d–q coordinate system can be reconstructed as

$$\begin{cases} \dot{\hat{x}} = \boldsymbol{A}\hat{\boldsymbol{x}} + \boldsymbol{B}\boldsymbol{u} + \boldsymbol{H}(y - \hat{y}) \\ \hat{y} = \boldsymbol{C}\hat{\boldsymbol{x}} \end{cases} \tag{27}$$

with

$$\boldsymbol{A} = \begin{bmatrix} -\frac{R_s}{L_d} & \frac{L_q}{L_d}\hat{\omega}_e \\ -\frac{L_q}{L_d}\hat{\omega}_e & -\frac{R_s}{L_q} \end{bmatrix};\ \boldsymbol{B} = \begin{bmatrix} \frac{1}{L_d} & 0 \\ 0 & \frac{1}{L_q} \end{bmatrix}$$

$$\boldsymbol{C} = \begin{bmatrix} \cos(\hat{\theta}_e - \frac{2\pi}{3}) & -\sin(\hat{\theta}_e - \frac{2\pi}{3}) \end{bmatrix};\ y = i_B$$

$$\boldsymbol{x} = \begin{bmatrix} i_d \\ i_q \end{bmatrix};\ \boldsymbol{H} = [h_1 \quad h_2]^T;\ \boldsymbol{u} = \begin{bmatrix} u_d \\ u_q - \hat{\omega}_e \psi_f \end{bmatrix}$$

where h_1 and h_2 denotes the specific gain coefficient, which should be designed to decrease the estimation error with time.

According to the rank criterion, the following condition in (28) can be met for (27) to ensure that the state variables i_d and i_q can be estimated

$$\operatorname{rank} \boldsymbol{V} = \operatorname{rank} \begin{bmatrix} \boldsymbol{C} \\ \boldsymbol{C}\boldsymbol{A} \\ \vdots \\ \boldsymbol{C}\boldsymbol{A}^{m-1} \end{bmatrix} = m \tag{28}$$

where m denotes the order of the matrix $\boldsymbol{A}$.

Therefore, the state variables i_d and i_q can be estimated by using the Luenberger observer in (27). By using (27), the d–q axis currents in phase-A CSF operation can be estimated as

$$\begin{cases} \dot{\hat{i}}_d = \frac{1}{L_d}(u_d - R_s\hat{i}_d + \hat{\omega}_e \frac{L_q}{L_d}\hat{i}_q) + h_1(i_B - \hat{i}_B) \\ \dot{\hat{i}}_q = \frac{1}{L_q}(u_q - R_s\hat{i}_q - \hat{\omega}_e \frac{L_d}{L_q}\hat{i}_d - \hat{\omega}_e \frac{\psi_f}{L_d}) + h_2(i_B - \hat{i}_B) \end{cases}. \tag{29}$$

By combining the estimated d–q axis currents and inverse Park transformation, the estimated phase-A current $\hat{i}_A$ can be estimated in phase-A CSF operation, and it can be denoted as

$$\hat{i}_A = \cos\hat{\theta}_e\hat{i}_d - \sin\hat{\theta}_e\hat{i}_q. \tag{30}$$

Finally, by using the estimated phase-A current $\hat{i}_A$ to replace the faulty current information, the FT control for phase-A CSF is fulfilled.

D. FT Control for VSF

After VSF, the measured dc-link voltage $U_{\mathrm{dc\_mea}}$ will deviate from the actual dc-link voltage $U_{\mathrm{dc\_act}}$, which will cause the estimation error of the rotor position and deteriorate the operation performance of the sensorless PMSM drive. To improve the post-fault performance in the sensorless PMSM drive, a voltage compensation-based FT control is proposed to tolerate the VSF in this article.

In Section II, the stator flux in α–β frame can be estimated by using the NFO in (7). Therefore, the stator flux amplitude can be estimated as

$$\psi_{\mathrm{est}} = \sqrt{\hat{\psi}_{s\alpha}^2 + \hat{\psi}_{s\beta}^2}. \tag{31}$$

In the NFO, the α–β stator voltage references are used to estimate the stator flux in α–β frame. After VSF, the α–β axis voltage references will deviate from the actual α–β axis voltage due to the incorrected $U_{\mathrm{dc\_mea}}$. Therefore, the estimation error will be generated between the estimated stator flux amplitude using (31) and the actual stator flux amplitude in VSF operation.

On the other hand, the d–q axis stator fluxes based on the PMSM model can be calculated as

$$\begin{cases} \psi_d = L_d i_d + \psi_f \\ \psi_q = L_q i_q \end{cases}. \tag{32}$$

According to (32), the calculated d–q axis stator fluxes ψ_d and ψ_q are only determined by the machine parameters and the d–q axis currents which will not be affected by the measured dc-link voltage in VSF operation. Therefore, the actual d–q axis stator fluxes ψ_d and ψ_q in VSF operation can still be calculated with (32) and the actual stator flux amplitude ψ_{act} can be calculated as

$$\psi_{\mathrm{act}} = \sqrt{\psi_d^2 + \psi_q^2}. \tag{33}$$

As aforementioned, the estimated stator flux amplitude ψ_{est} will deviate from the actual stator flux amplitude ψ_{act} in VSF operation. To eliminate the error between the estimated stator flux amplitude ψ_{est} and the actual stator flux amplitude ψ_{act}, the actual dc-link voltage should be obtained to replace the measured dc-link voltage $U_{\mathrm{dc\_mea}}$. According to (7) and (31), the estimated stator flux amplitude ψ_{est} is positively related to the α–β stator voltage. Meanwhile, the α–β stator voltage are also positively related to the measured dc-link voltage $U_{\mathrm{dc\_mea}}$. As a result, the estimated stator flux amplitude ψ_{est} is positively related to the measured dc-link voltage $U_{\mathrm{dc\_mea}}$. Therefore, a PI controller is introduced to generate the compensated dc-link voltage $U_{\mathrm{dc\_com}}$ in VSF operation, which can eliminate the error between the estimated stator flux amplitude ψ_{est} and the actual stator flux amplitude ψ_{act}, as shown in Fig. 6. By adding the compensated dc-link voltage $U_{\mathrm{dc\_com}}$ into the measured dc-link voltage $U_{\mathrm{dc\_mea}}$, the actual dc-link voltage can be estimated. By replacing the measured dc-link voltage $U_{\mathrm{dc\_mea}}$ with the estimated dc-link voltage U_{dc_est}, the VSF can be tolerated, and the error between the estimated stator flux amplitude ψ_{est} and the calculated stator flux amplitude ψ_{cal} can be eliminated.

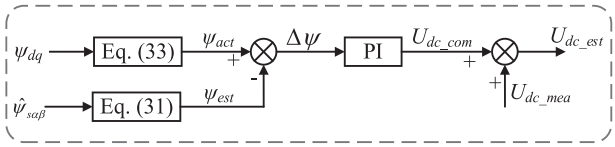

Fig. 6. Estimation of the actual DC-link voltage.

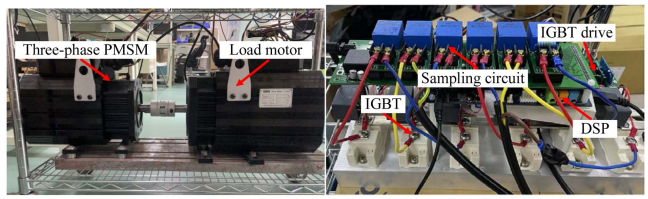

Fig. 7. Experimental platform. (a) Motor. (b) Inverter.

TABLE I
PARAMETERS OF EXPERIMENTAL SETUP

Parameter	Value
Number of pole pairs	4
Stator resistance	0.93 Ω
d-axis inductance	6.26 mH
q-axis inductance	6.26 mH
Load torque	8.7 Nm
PM flux-linkage	0.3 Wb
DC-link voltage	200 V
Given speed	600 r/min
Switching frequency	10 kHz

V. EXPERIMENTAL VERIFICATIONS

To verify the proposed FTC scheme, the experimental platform is established, as shown in Fig. 7. The platform mainly includes a three-phase PMSM, a load motor, and hardware circuits. The PMSM and load motor are coupled together by using the couplings. The sensorless control of PMSM drive and the proposed FT control scheme is performed with DSP (TMS320F28335). The key parameters of the experimental platform are given in Table I. In the experiment, OPF is achieved by opening the breaker of the faulty phase. OSF is simulated by imposing the driving signal of the faulty switch to be low constantly. CSF and VSF are realized by changing the feedback values of the current sensor and voltage sensor, respectively.

Fig. 8 presents the fault operation of the proposed sensorless control for PMSM drive in phase-A OPF. In Fig. 8(a), the phase-A current is forced to zero, and the remaining two phase currents remain opposite after phase-A OPF. By using the calculated α–β stator voltages in the NFO, the rotor position can be estimated accurately, and the maximum estimation error of the rotor position is about 0.21 rad, as shown in Fig. 8(b). It can be seen from Fig. 8 that the PMSM can operate continually in Phase-A OPF by using the proposed sensorless control, and the precision rotor position can be estimated.

Fig. 9 shows the performance of the proposed FT control using $i*$ $B2$ in phase-A OPF. In phase-A OPF FT operation, the phase-A current is zero, and the patterns of the remaining two

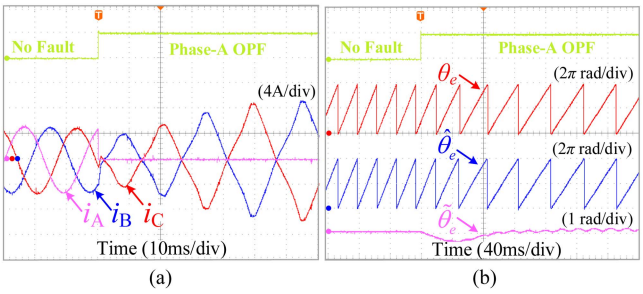

Fig. 8. Fault operation of the proposed sensorless control for the PMSM drive in phase-A OPF. (a) Three-phase currents. (b) Rotor positions.

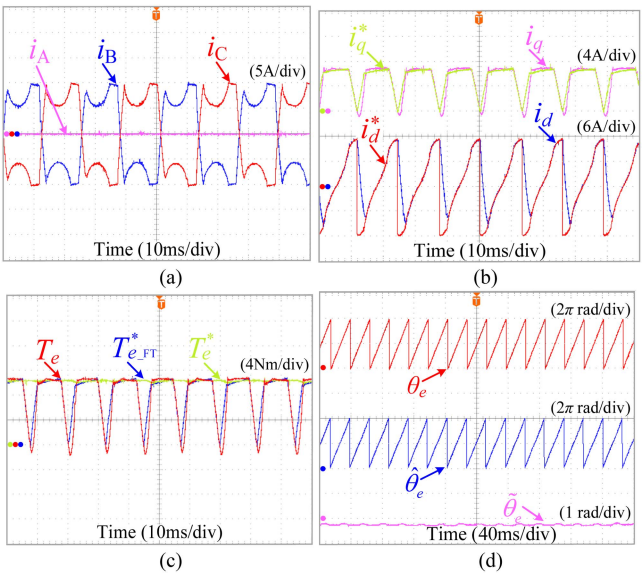

Fig. 9. Performance of the proposed FT control using $i*$ $B2$ in phase-A OPF. (a) Three-phase currents. (b) d–q axis currents. (c) Torques. (d) Rotor positions.

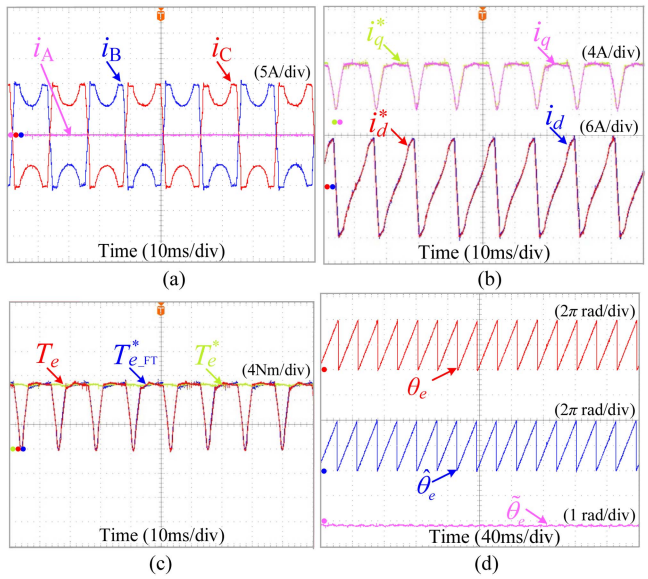

Fig. 10. Performance of the proposed FT control using $i*$ $B4$ in phase-A OPF. (a) Three-phase currents. (b) d–q axis currents. (c) Torques. (d) Rotor positions.

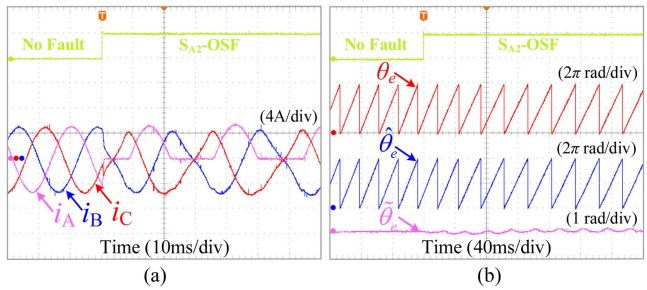

Fig. 11. Fault operation of the proposed sensorless control for the PMSM drive in phase-A OPF. (a) Three-phase currents. (b) Rotor positions.

phase currents are identical, as shown in Fig. 9(a). In Fig. 9(b), the tracking errors between the d–q axis currents and their references are obvious since the desirable current commutation time is not considered. Similarly, the torque output T_e cannot also track the FT torque reference $T*$ e_FT, and the negative torque is generated, as shown in Fig. 9(c). Moreover, the maximum value of the FT torque reference $T*$ e_FT is equal to the torque reference $T*$ e according to (16). In Fig. 9(d), the rotor position of the PMSM can still be estimated accurately by using the proposed sensorless control in phase-A OPF FT operation.

In Fig. 10, the performance of the FT control using $i*$ $B3$ is presented in phase-A OPF. Compared with Fig. 9(a), the desirable current commutation time is considered, as shown in Fig. 10(a). In Fig. 10(b), the d–q axis currents can track their references precisely. In Fig. 10(c), the negative torque and the tracking error between the torque output T_e and the FT torque reference $T*$ e_FT is eliminated effectively. In Fig. 10(d), the rotor position is still estimated accurately. It should be noted that the torque ripple in Fig. 10(c) is inevitable for in the three-phase sensorless PMSM drive due to the loss of the faulty phase. Moreover, the torque reference $T*$ e generated by the speed PI controller is used as the maximum value of the FT torque output $T*$ e_FT. Therefore, the torque reference $T*$ e is higher than the load torque.

In Fig. 11, the fault operation of the proposed sensorless control for PMSM drive is presented in the S_{A2}-OSF. In Fig. 11(a), the three-phase currents remain the sinusoidal waveforms in the healthy half fundamental period. In the faulty half fundamental period, the system switches to the OPF operation. In Fig. 11(b), the rotor position in S_{A2}-OSF operation can be estimated accurately by using the proposed sensorless control.

Fig. 12 presents the performance of the proposed FT control using (25) in S_{A2}-OSF. The three-phase currents remain normal in the healthy half fundamental period and switch to the phase-A OPF FT operation in the faulty half fundamental period, as shown in Fig. 12(a). In Fig. 12(b) and (c), the torque and d–q axis currents can also track their references precisely. Compared with Fig. 10(c), the torque ripple is decreased obviously by using the remaining healthy switch to improve the FT performance in S_{A2}-OSF FT operation, as shown in Fig. 12(c). In Fig. 12(d), the desirable performance of the estimated rotor position can still be guaranteed.

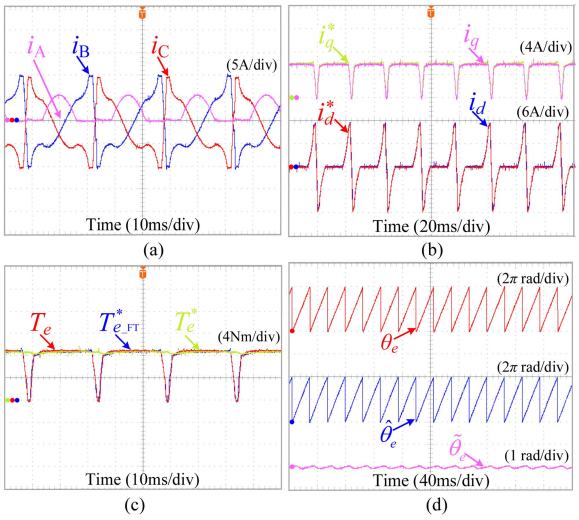

Fig. 12. Performance of the proposed FT control in S_{A2}-OSF considering the current commutation. (a) Three-phase currents. (b) *d*–*q* axis currents. (c) Torques. (d) Rotor positions.

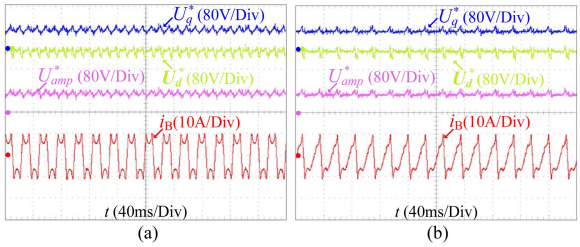

Fig. 13. *dq*-axis voltage references in phase-A OPF and S_{A2}-OSF FT operations: (a) Phase-A OPF. (b) S_{A2}-OSF.

Fig. 13 presents the *dq*-axis voltage references in phase-A OPF and S_{A2}-OSF FT operations. It can be found that small voltage ripples are generated in the *dq*-axis voltage references and its amplitude $U*$ amp in phase-A OPF and S_{A2}-OSF FT operations since the *dq*-axis current references contain low-order harmonics. Due to the occurrence of small voltage ripples in phase-A OPF and S_{A2}-OSF FT operations, the maximum values of the *dq*-axis voltage references are increased slightly in phase-A OPF and S_{A2}-OSF FT operations compared with normal operation. As a result, the upper limitation of the motor speed will be decreased slightly in phase-A OPF and S_{A2}-OSF FT operations, which is acceptable in practical FT operation.

Fig. 14 presents the performance of the proposed FT control in phase-A CSF. After CSF, the faulty current of the phase-A current sensor is replaced by using the estimated current, and the actual three-phase currents are still the sinusoidal waveforms with normal operation in phase-A CSF FT operation, as shown in Fig. 14(a). In Fig. 14(b), the estimated phase-A current is almost identical to the actual phase-A current, and the maximum error between the estimated current and the actual current is always less than 1A in phase-A CSF FT operation. Meanwhile, the satisfactory performance of the rotor position

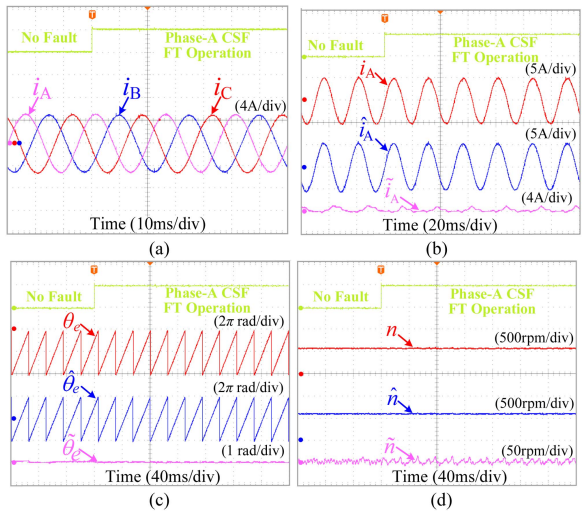

Fig. 14. Performance of the proposed FT control in phase-A CSF. (a) Three-phase currents. (b) Estimated phase-A current. (c) Rotor positions. (d) Speeds.

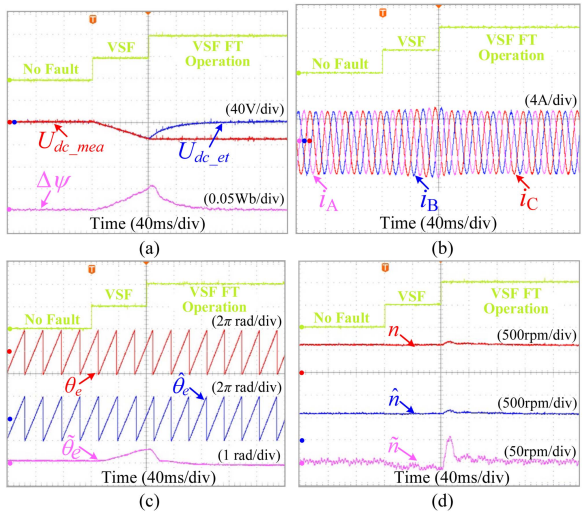

Fig. 15. Performance of the proposed FT control in Phase-A VSF. (a) DC-link voltages. (b) Three-phase currents. (c) Rotor positions. (d) Speeds.

estimation and speed estimation are still remained, as shown in Fig. 14(c) and (d).

In Fig. 15, the performance of the proposed FT control for VSF is presented. After VSF, the error of the measured voltage is increased from 0% to 20% within 80 ms, as shown in Fig. 16(a). In Fig. 15(b), the amplitude of the three-phase currents is increased slightly in the VSF operation. In Fig. 15(a), the flux error $\Delta\psi$ between the estimated flux amplitude $\psi_{\rm est}$ and the actual flux amplitude $\psi_{\rm act}$ is also increased gradually. In Fig. 15(c) and Fig. 15(d), the rotor position and speed estimation error are increased in VSF operation. After the FT control of the VSF is fulfilled, the compensated dc-link voltage $U_{\rm dc\_com}$ is generated based on the flux error $\Delta\psi$, which is added to the measured dc-link voltage $U_{\rm dc\_mea}$ to obtain the estimated dc-link voltage $U_{\rm dc\_est}$. Meanwhile, the estimated dc-link voltage $U_{\rm dc\_est}$ is used to replace the measured dc-link voltage U_{dc_mea}

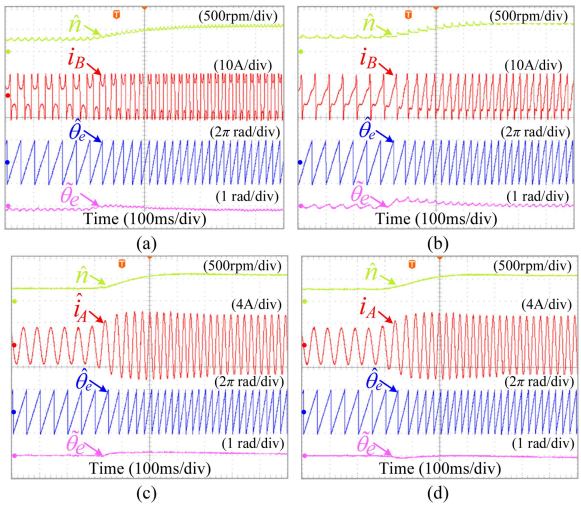

Fig. 16. Transient performance of the proposed FT control in different operations. (a) Phase-A OPF opeation. (b) S_{A2}-OSF operation. (c) Phase-A CSF operation. (d) VSF operation.

in the sensorless PMSM drive. The estimated dc-link voltage $U_{\mathrm{dc\_est}}$ can track the actual dc-link voltage gradually, as shown in Fig. 15(a). In this process, the flux error $\Delta\psi$ is decreased gradually in Fig. 15(b). In Fig. 15(c) and (d), the estimation errors of the rotor position and speed will be eliminated gradually in the VSF operation and return to the low level.

Fig. 16 shows the transient performance of the proposed FT control in different operations with the speed step from 300 to 600 r/min. In phase-A OPF and S_{A2}-OSF operations, the proposed FT control can still drive the motor normally when the speed changes, and the smooth transiation can be obtained, as shown in Fig. 16(a) and (b). In phase-A CSF, the phase-A current can be estimated accurately to realize the FT control of phase-CSF with the speed step, as shown in Fig. 16(c). In Fig. 16(d), the phase-A current remains normal sinusoidal waveforms with the speed step, which determine the measured voltage error can still be compensated accurately. Although the estimation error of the rotor position is increased slightly when the speed changes in these FT operations, the error level is acceptable and always less than 0.4 rad. Moreover, when the speed stabilizes, the estimation error will return to the low level. It can be seen from Fig. 16 that the proposed FTC scheme possesses good roubustness against the transient performance in the sensorless PMSM drive.

VI. Conclusion

In this article, an FT control scheme is proposed for four types of faults in the sensorless PMSM drive, namely OPF, OSF, CSF, and VSF. First, both the rotor position is estimated accurately in OPF and OSF operations by using the calculated α–β stator voltages for the voltage inputs of the NFO. Based on the estimated rotor position in OPF and OSF operations, the current commutation is considered to optimize the FT current reference. By using the optimized FT current reference, the current tracking errors and negative torque are eliminated effectively. Second, the current information of the faulty phase current sensor is estimated by using the reconstructed Luenberger observer to complete the FT control for CSF. Finally, the FT control of VSF is realized by compensating the measured voltage error based the flux error between the estimated flux amplitude and actual flux amplitude. The experiments prove the effectiveness of the proposed FT control scheme.

References

[1] A. Balamurali, G. Feng, A. Kundu, H. Dhulipati, and N. C. Kar, "Non-invasive and improved torque and efficiency calculation toward current advance angle determination for maximum efficiency control of PMSM," *IEEE Trans. Transp. Electrific.*, vol. 6, no. 1, pp. 28–40, Mar. 2020.

[2] Y. Zhang, Y. Mao, X. Wang, Z. Wang, D. Xiao, and G. Fang, "Current prediction-based fast diagnosis of electrical faults in PMSM drives," *IEEE Trans. Transp. Electrific.*, vol. 8, no. 4, pp. 4622–4632, Dec. 2022.

[3] B. Luo, X. Yang, and Y. Zhou, "Model-free predictive current control of permanent magnet synchronous motor based on estimation of current variations," *IEEE Trans. Ind. Electron.*, vol. 71, no. 8, pp. 8395–8405, Aug. 2024.

[4] D. Xiao et al., "Universal full-speed sensorless control scheme for interior permanent magnet synchronous motors," *IEEE Trans. Power Electron.*, vol. 36, no. 4, pp. 4723–4737, Apr. 2021.

[5] M. Hasegawa, S. Yoshioka, and K. Matsui., "Position sensorless control of interior permanent magnet synchronous motors using unknown input observer for high-speed drives," *IEEE Trans. Ind. Appl.*, vol. 45, no. 3, pp. 938–946, May–Jun. 2009.

[6] D. Xiao et al., "Computation-efficient position estimation algorithm for permanent magnet synchronous motor drives under distorted conditions," *IEEE J. Emerg. Sel. Top. Power Electron.*, vol. 9, no. 3, pp. 2759–2773, Jun. 2021.

[7] Z. Wu, C. C. W.Hua, H. Zhang, and M. Hu, "A square-wave voltage injection sensorless control for dual three-phase IPMs robust to open circuit faults," *IEEE Trans. Ind. Electron.*, vol. 71, no. 2, pp. 1113–1124, Feb. 2023.

[8] X. Zhou, J. Sun, H. Li, M. Lu, and F. Zeng, "PMSM open-phase fault-tolerant control strategy based on four-leg inverter," *IEEE Trans. Power. Electron.*, vol. 35, no. 3, pp. 2799–2808, Mar. 2020.

[9] A. Kiselev, G. R. Catuogno, A. Kuznietsov, and R. Leidhold, "Finite-control-set MPC for open-phase fault-tolerant control of PM synchronous motor drives," *IEEE Trans. Ind. Electron.*, vol. 67, no. 6, pp. 4444–4452, Jun. 2020.

[10] R. R. Errabelli and P. Mutschler, "Fault-tolerant voltage source inverter for permanent magnet drives," *IEEE Trans. Power Electron.*, vol. 27, no. 2, pp. 500–508, Feb. 2012.

[11] J. Shen, X. Wang, D. Xiao, Z. Wang, Y. Mao, and M. He, "Online switching strategy between dual three-phase PMSM and open-winding PMSM," *IEEE Trans. Transport. Electrific.*, vol. 10, no. 1, pp. 1519–1529, Mar. 2024, doi: 10.1109/TTE.2023.3289973.

[12] Z. Zhang, X. Wang, D. Xiao, Y. Zhou, M. He, and Z. Wang, "A novel 3D space vector modulation strategy for open-end winding PMSM," *IEEE Trans. Ind. Electron.*, vol. 71, no. 8, pp. 8536–8547, Aug. 2024, doi: 10.1109/TIE.2023.3314868.

[13] Y. Chen, X. Wang, X. Meng, M. He, D. Xiao, and Z. Wang, "A universal model predictive control strategy for dual inverters fed OW-PMSM drives," *IEEE Trans. Power Electron.*, vol. 38, no. 6, pp. 7575–7585, Jun. 2023.

[14] W. Huang, X. Zhu, H. Zhang, and W. Hua, "Generalized fault-tolerant model predictive control of five-phase PMSM drives under single/two open-switch faults," *IEEE Trans. Ind. Electron.*, vol. 70, no. 8, pp. 7569–7579, Aug. 2023.

[15] L. Jin, Y. Mao, X. Wang, L. Lu, and Z. Wang, "Online data-driven fault diagnosis of dual three-phase PMSM drives considering limited labeled samples," *IEEE Trans. Ind. Electron.*, vol. 71, no. 7, pp. 6797–6808, Jul. 2024, doi: 10.1109/TIE.2023.3312431.

[16] M. Tousizadeh, H. S. Che, J. Selvaraj, N. A. Rahim, and B. Ooi, "Performance comparison of fault-tolerant three-phase induction motor drives considering current and voltage limits," *IEEE Trans. Ind. Electron.*, vol. 66, no. 4, pp. 2639–2648, Apr. 2019.

[17] M. Aleenejad, H. Iman-Eini, and S. Farhangi, "Modified space vector modulation for fault-tolerant operation of multilevel cascaded H-bridge inverters," *IET Power. Electron.*, vol. 6, no. 4, pp. 742–751, Apr. 2013.

[18] J. Li, A. Q. Huang, Z. Liang, and S. Bhattacharya, "Analysis and design of active NPC (ANPC) inverters for fault-tolerant operation of high-power electrical drives," *IEEE Trans. Power. Electron.*, vol. 27, no. 2, pp. 519–533, Feb. 2012.
[19] A. Kontarček, P. Bajec, M. Nemec, V. Ambrožič, and D. Nedeljković, "Cost-effective three-phase PMSM drive tolerant to open-phase fault," *IEEE Trans. Ind. Electron.*, vol. 62, no. 11, pp. 6708–6718, Nov. 2015.
[20] Z. Zhang, Y. Hu, G. Luo, C. Gong, X. Liu, and S. Chen, "An embedded fault-tolerant control method for single open-switch faults in standard PMSM drives," *IEEE Trans. Power. Electron.*, vol. 37, no. 7, pp. 8476–8487, Jul. 2022.
[21] X. Wang, Z. Wang, M. Gu, B. Wang, W. Wang, and M. Cheng, "Current optimization-based fault-tolerant control of standard three-phase PMSM drives," *IEEE Trans. Energy Convers.*, vol. 36, no. 2, pp. 1023–1035, Jun. 2021.
[22] X. Wang, S. Ren, D. Xiao, X. Meng, G. Fang, and Z. Wang, "Fault-tolerant control of open-circuit faults in standard PMSM drives considering torque ripple and copper loss," *IEEE Trans. Transport. Electrific.*, vol. 10, no. 2, pp. 4239–4251, Jun. 2024, doi: 10.1109/TTE.2023.3306457.
[23] Y. Zhang, X. Chen, X. Wang, T. Zhang, Z. Wang, and Y. Mao, "Online current optimization-based fault-tolerant control of standard PMSM drives," *IEEE Trans. Ind. Electron.*, vol. 71, no. 12, pp. 15521–15531, Dec. 2024, doi: 10.1109/TIE.2024.3398673.
[24] G. Zhang, H. Zhou, G. Wang, C. Li, and D. Xu, "Current sensor dault-tolerant control for encoderless IPMSM drives based on current space vector error reconstruction," *IEEE J. Emerg. Sel. Topics Power Electron.*, vol. 8, no. 4, pp. 3658–3668, Dec. 2020.
[25] G. Wang, X. Hao, N. Zhao, G. Zhang, and D. Xu, "Current sensor fault-tolerant control strategy for encoderless PMSM drives based on single sliding mode observer," *IEEE Trans. Power. Electron.*, vol. 6, no. 2, pp. 679–689, Jun. 2020.
[26] S. K. Kommuri, S. B. Lee, and K. C. Veluvolu, "Robust sensors-fault-tolerance with sliding mode estimation and control for PMSM drives," *IEEE/ASME Trans. Mechatron.*, vol. 23, no. 1, pp. 17–28, Feb. 2018.
[27] J. Lee, J. Hong, K. Nam, R. Ortega, L. Praly, and A. Astolfi, "Sensorless control of surface-mount permanent-magnet synchronous motors based on a nonlinear observer," *IEEE Trans. Power Electron.*, vol. 25, no. 2, pp. 290–297, Feb. 2010.
[28] Z. Li et al., "A fast diagnosis method for both IGBT faults and current sensor faults in grid-tied three-phase inverters with two current sensors," *IEEE Trans. Power Electron.*, vol. 35, no. 5, pp. 5267–5278, May 2020.
[29] X. Zhou, Q. Hu, P. Cui, X. Xu, and K. Mao, "A fast open-switch fault and open-winding fault distinguish method based on voltage reference modification," *IEEE Trans. Power Electron.*, vol. 38, no. 9, pp. 11451–11462, Sep. 2023.
[30] F. Mehmood, P. M. Papadopoulos, L. Hadjidemetriou, A. Charalambous, and M. M. Polycarpou, "Model-based fault diagnosis scheme for current and voltage sensors in grid side converters," *IEEE Trans. Power Electron.*, vol. 38, no. 4, pp. 5360–5375, Apr. 2023.

Yun Zhang (Student Member, IEEE) received the B.E. degree in machine engineering college from Dalian maritime University, Dalian, China, in 2021. He is currently working toward the Ph.D. degree in measuring technology and instrument with the Institute of Optics and Electronics, Chinese Academy of Science, Chengdu, China.

His current research interests include the fault diagnosis and fault-tolerant operation of permanent-magnet motor drives.

Xueqing Wang (Senior Member, IEEE) received the B.S. degree in electrical engineering from Tianjin University of Science and Technology, Tianjin, China, in 2014, and the M.S. and Ph.D. degrees from Southeast University, Nanjing, China, in 2016 and 2020, respectively, both in electrical engineering.

From 2018 to 2019, he was a joint Ph.D. with McMaster Automotive Resource Centre, McMaster University, Hamilton, ON, Canada. He is currently an Associate Research Fellow with the College of Electrical Engineering, Sichuan University, Chengdu, China. His research interests include control of multiphase motor and open-winding motor, fault diagnosis and tolerant control of motor drive, multilevel PWM strategy.

Lei Kong (Student Member, IEEE) received the B.E. degree in marine engineering from Dalian Maritime University, Dalian, China, in 2022. He is currently working toward the M.E. degree in measuring technology and instrument with the University of Chinese Academy of Sciences, Institute of Optics and Electronics, Chinese Academy of Sciences, Chengdu, China.

His research interests include fault diagnosis of permanent-magnet synchronous motor drives, multilevel inverters, and nonlinear compensation.

Linlin Lu (Student Member, IEEE) received the B.E. degree in communication engineering from Zhengzhou University, Zhengzhou, China, in 2021. She is currently working toward the Ph.D. degree in measuring technology and instrument with the Institute of Optics and Electronics, Chinese Academy of Science, Chengdu, China.

Her current research interests include the loss optimization and fault-tolerant control of motor drives and manipulators.

Zheng Wang (Senior Member, IEEE) received the B.Eng. and M.Eng. degrees in electrical engineering from Southeast University, Nanjing, China, in 2000 and 2003, respectively, and the Ph.D. degree in electrical engineering from The University of Hong Kong, Hong Kong, in 2008, all in electrical engineering.

From 2008 to 2009, he was a Postdoctoral Fellow in Ryerson University, Toronto, ON, Canada. He is currently a full Professor with the School of Electrical Engineering, Southeast University. He has authored or coauthored more than 80 internationally refereed papers and four books in these areas. His research interests include electric drives, power electronics, and distributed generation.

Yao Mao (Senior Member, IEEE) received the B.S. degree in automatic control from the Department of Automation, Chongqing University, China, in 2001, and the Ph.D. degree in signal and information processing from the Institute of Optics and Electronics, Chinese Academy of Science, in 2012.

He has been a Professor with the University of Chinese Academy of Sciences since 2016. His research interests include power electronics, motion control, information fusion, machine learning.

Dr. Mao was the recipient of Distinguished Scientific Achievement Award by the Chinese Academy of Science in 2011.